

## DETECTION OF LANDSLIDES WITH SAR POLARIMETRY: CASE STUDY OF SOUTH-EASTERN COLOMBIA

N. A. Correa-Muñoz<sup>1\*</sup>, C. A. Murillo-Feo<sup>2</sup>

<sup>1</sup> Faculty of Civil Engineering, Universidad del Cauca, Popayán, Colombia. PhD Student of Engineering Faculty, Universidad Nacional de Colombia - nico@unicauca.edu.co, nacorrean@unal.edu.co

<sup>2</sup> Department of Civil and Agricultural Engineering, Universidad Nacional de Colombia, Bogotá, Colombia - camurillof@unal.edu.co

### Commission VI, WG VI/4

**KEY WORDS:** Backscattering Coefficient, Dispersion Mechanism, Landslides, Polarimetry SAR (PolSAR), Entropy – Alpha Parameter Classification, Principal Component Analysis

### ABSTRACT:

SAR polarimetry (PolSAR) is a method that can be used to investigate landslides. Polarimetric scattering power decomposition allows to separate the total power received by the SAR antenna, which is divided in surface scattering power, double bounce scattering and volume scattering power. Polarimetric indices are expected to serve for landslide recognition, because landslides' scattering properties are different from those of the surrounding forested areas. The surface scattering mechanism is mainly caused by rough surfaces like bare soil and agricultural fields, so we hope that this will be the predominant dispersion mechanism in landslides. In a study area located in south-western Colombia, we used dual-Pol provided by ESA's Sentinel-1 satellites and quad-pol from NASA's UAVSAR aerial platform. Using C-band and L-band radar images, we analysed the interaction between radar signals and landslides. First, with dual-pol we found backscatter calibrate coefficients over four GRD radar images acquired between 2015 and 2017. The analysis gave an average backscatter value of -14.47 dB for VH polarisation and -8.40 dB for VV polarisation. Then, using H-a decomposition for quad-pol data, we validated the high relationship between entropy and alpha parameter, which has the highest contribution to the first axis in a principal component analysis. These results were used to obtain an unsupervised classification of landslides, that separated the Colombian Geological Service landslide inventory in three classes characterized by the mechanism of dispersion. These results will be combined with InSAR parameters, morphometric parameters and optical spectral indexes to obtain a local detection model of landslides.

### 1. INTRODUCTION

The radar is a system that uses electromagnetic waves (microwaves) to observe and to exam all kind of objects located in the Earth's surface. Furthermore, it is used to determine the distance between an object positioned in the surface and the radar itself. It emits signals in different incident angles that when reaches an object, the time that the echo takes on coming back to the radar is interpreted as the distance between them (Richards, 2009). The backscatter energy represents the amplitude and intensity of the wave (Rocca et al., 2014). It is also characterized as an oblique system, because if the signal was to be transmitted straight down towards the the surface, all echoes would return to the radar at the same time, without having the possibility of making signal differentiations. As it doesn't always takes measures over flat surfaces, the ground topography generates problems in geometric parameters: radar shadow (steep slopes oriented far from SAR return no signal), fore shortening (the slopes oriented to the SAR appears compressed) and lay over (steep slopes oriented to the SAR lead to ghost images) (Colesanti et al., 2006).

Landslides are topographic grounds that can be found due to natural formations, and it's very important to examine them because they causes human casualties and could damage infrastructures (Sun et al., 2017). These landslides were

classified considering the three principal scattering mechanisms obtained when measuring the Earth's surface over electromagnetic field's alignment, with the final purpose of differentiating all objects on the ground. One of them is surface scattering (the waves hit a homogenous surface and some of the energy is returned to the radar), double bounce scattering (it's the dominant mechanism over man-made structure; in comparison to surface scattering, the wave hits two perpendicular objects and the intensity of the wave doesn't change at any time), and volume scattering (occurs principally in forest canopies; the signal is weaker because the wave is scattered and only a few energies are sent back to the radar).

The objective of this research is to understand and to distinguish the mechanisms of interaction between radar energy and terrestrial objects, specifically the scatters related to the landslides. This was achieved through the analysis of radar intensity signal and the decomposition of radar signal.

### 2. THEORETICAL FRAMEWORK

A radar image is a product acquired by a satellite in the microwave electromagnetic spectrum (Matikainen et al., 2016). The technique of this product is obtained by Synthetic Aperture Radar (SAR), which is based on the use of the Doppler shift in the echoes to achieve a much higher spatial resolution. SAR

\* Corresponding author

describes an engineering method that is used to achieve higher resolution radar image and it's produced by using the forward motion of the radar. In addition, SAR has the capability of sending out and receiving electromagnetic information about the targets on the ground, illuminated by the microwave pulses (Scaioni et al., 2014; Shibayama et al., 2015).

A satellite emits a radar signal representing a complex number of the amplitude and phase of a wave (Tessari et al., 2017). The satellite has the advantage of taking images at any time of the day; it does not depend on weather conditions because the signal has an atmospheric transparency, and it also possesses wide coverage (Plank et al., 2016; Tehrani et al., 2017).

## 2.1 Parameters that determine the intensity of the returned energy to the radar

These can be divided into two groups: sensor parameters (incident angle of the wave, wavelength, and spatial resolution), and ground parameters (topography, surface roughness, and the water content of the ground) (Matikainen et al., 2016).

### 2.1.1 Sensor parameters

The radar is an oblique sight where the echoes that come back from the ground surface exist in proportion to the distance along the ground. The azimuth direction is the projection on the ground of the path travelling of the sensor satellite board. In the range direction, the radar can oversee at different angles or incidence angles, which is defined between the normal to the surface and the direction from the sensor to the ground (Notti et al., 2010). If the swath is the area that can be covered on the ground by the sensor, then the incidence angle can be different at the near side of the swath to the far side of the swath. This brings as consequence that microwaves interact with the surface in a very different way, depending on the local topography.

Another sensor parameter of the radar system is the wavelength. Normally, in radar the X-band (8 – 12 GHz | 2.5 -3.75 cm), i.e. COSMO Skymed, C-band (4 – 8 GHz | 3.75 -7.5 cm), i.e. Sentinel-1, L-band (0.5– 1.5 GHz | 20 – 60 cm), i.e. ALOS PalSAR, and P-band (0.25 – 0.5 GHz | 60 – 120 cm), i.e. Biomass, are used (Richards, 2009). The longest wavelength allows to see deeper into the forest canopy. In overall terms, the microwaves interact with objects whose size is approximately on the same scale as the wavelength. In other words, a tree can look very different, depending on the radar wavelength the satellite is using. For example, X-band detects leaves and twigs, C-band leaves or small branches, L-band branches, and P-band branches and trunks (Vogeler et al., 2016). The spatial resolution can influence in the accuracy of the final product and it has an indirect relationship with wavelength, being the resolution (azimuth x range) higher for the X-band (1 by 1 m resolution), C-band (5 by 5 m resolution), L-band (10 by 10 m resolution) (Casagli et al., 2017; Ouchi, 2013).

### 2.1.2 Ground parameters

The topography of the earth's surface causes disturbances on radar images (Tessari et al., 2017) like radar shadow, foreshortening, and layover. Radar shadow is a very common problem on very steep mountains with large incidence angle illumination. Due to the side-looking geometry, the back side, which faces away from the sensor- is not visible to the radar

system, hence no information can be collected (Colesanti et al., 2006). If the signals are sent at the front of a building, the region behind it will not reflect any signal, so an obscure region is shown on the image. We can fix radar shadow by using a digital elevation model to reconstruct all geometric errors (Wilson, 2012). Another geometric distortion is foreshortening; on this case the terrain slopes looking directly to the radar are schematized as having a compressed scale related to its appearance (Colesanti et al., 2006). Foreshortening is caused by the side-looking geometry of the radar system in mountainous areas. The hill slopes facing the sensor appear very bright. The effect is more pronounced for steeper slopes and for radars that use steeper incidence angles. The last parameter is layover: when targets appear to lean over in an image. This is because one dimension of a radar image is constructed based on the echoes' delay. The effect is more pronounced for steeper slopes and for radars that use smaller incidence angles. Knowing the height of the satellite and with the constant velocity of light, this error can be corrected (Adiri et al., 2017).

Surface roughness and water content, also known as dielectric constant, are related to each other. If we want to obtain back as much energy of the wave as it's possible, the highest are these two parameters, the better it will be. For example, let's pretend a radar image of a field is going to be taken, if the field is a flat surface, the signals are going to be reflected away and they will not return to the antenna, this is a process called specular reflection. On the other hand, in a rough surface occurs a diffuse reflection, the wave scatters when it hits all kind of inclined surfaces, so some of this energy is received by the antenna. Now let's imagine if it is a rough surface and contains a lot of water, more signals will be returned and because the water helps the signal to penetrate the ground, and hence more diffusion of the signal occurs. A study to determine and monitor soil moisture in drylands from C-band SAR images like function on surface topography is found in Tansey & Millington (2001). Ouchi (2013) explains the models used to estimate the soil moisture with prior knowledge of surface roughness.

## 2.2 Characteristics of a radar image

A radar image has diverse types. The Single Look Complex (SLC) which includes the amplitude and the phase of the data, and Ground Range Detected (GRD) images, which includes only the amplitude, are the ones this research is focusing on. This kind of images are products obtained by level 1, meaning that they were processed with algorithms and calibration data. The processing involved to produce Level-1 data products includes pre-processing, Doppler centroid estimation, single look complex focusing, and image and post-processing to generate SLC and GRD products as well as mode specific processing for assembling of multi-swath products. SLC images allow to produce interferograms of high quality by co-registration of master and slave radar images (García-Davalillo et al., 2014). To obtain a radar image, the Interferometric Wide Swath (IWC) mode is helpful because it possesses not only a single polarisation mode but two (dual) polarisations, and it has a spatial resolution of 5 by 20m. This is obtained from TOPS SAR acquisition which eliminates the problems associated with ScanSAR technique (Yague-martinez et al., 2016).

The polarisation modes consist on how the radar signal is emitted to the object and how it is reflected, which could be transmitted horizontally or vertically, and receive the wave in

the same direction (co-polarisation, HH or VV), or it could also be receiving in a different direction as it was emitted (cross-polarisation, HV or VH) (Yonezawa et al., 2012). The HH is used for wetland detection, the VV for soil moisture and flood conditions (Mahdianpari et al., 2017), and cross-polarisation is very useful to estimate the soil properties (Han et al., 2017). According to Shimada et al. (2014) the thresholds for HH and HV polarisation for separating forest and non-forest were -6.89 dB in HH and -12.07 dB in HV using L-band backscatter.

The radar polarimetry is a very useful technique to understand the scattering mechanism of different targets on the Earth's surface and it studies and measures the direction of the radar signal. The polarisation state of a backscattered wave from a natural surface can be linked to geometrical characteristics like shape, roughness and orientation and the intrinsic properties of the scattered like humidity/moisture, salinity or medium density. The polarisation is a property of electromagnetic radiation where the wave has an orientation that can be horizontally or vertically transmitted and received (Ouchi, 2013). Depending on the Earth's surface slope or the orientation of the objects, the polarisation can help to interpret what the surface characteristics are. Using polarimetry, it's possible to determine which scattering mechanism is occurring in a topography field (Shibayama et al., 2015). One way to determine the scattering mechanisms is with the method of decomposition of the alpha and entropy values of the wave. By combining these values, a bi-dimensional graphic can be obtained and it provides information about the mechanism of interaction of an object in the ground (Yonezawa et al., 2012). The graphic is divided in 9 zones, being the 7th and 4th zones equal to double bounce scattering, 8th, 5th and 2th corresponds volume scattering, and 9th, 6th and 3th belong to surface scattering (zone 1 is a no feasible zone). The entropy values are given in a range between 0 and 1, knowing that an entropy between 0 to 0.5 is equal to the probability that it exists only one scattering mechanism, and an entropy between 0.5 to 1 is equal to the probability that all three-scattering mechanism exist in the same pixel. Similarly, the alpha values are represented by angles (0° - 90°). The predominant scattering mechanism between 0 to 41 degrees is surface dispersion, 41 to 47 degrees volume dispersion, and 47 to 90 degrees double bounce dispersion (Li et al., 2017).

### 3. METHODOLOGY AND DATA

#### 3.1 Methodology

##### 3.1.1 Dual Pol

With the aid of the Alaska Satellite Facility platform (<https://www.asf.alaska.edu/>), four images obtained with C-band, and with VV and VH polarisations each one, were downloaded: S1A 1C60 (acquired on May 12th, 2015), S1B 2EDC (Nov 20th, 2016), S1B BA6C (Aug 11th, 2017), and S1B 9006 (Sep 30th, 2017). These images were analysed with the Sentinel Application Platform (SNAP) software of the European Space Agency. The images were calibrated to reduce the speckle noise and to correct the terrain, to make possible to obtain the backscattering coefficient of all of them (Mondini, 2017). The backscattering coefficient represents the amplitude of the wave, which takes extremely high values, for that reason it was very important to convert the values to decibels (dB) (Richards, 2009). After having the backscattering coefficient, another software called R software environment (<http://www.r-project.org/>) was used to create a boxplot figure (Figure 2) showing the differentiation of the polarisations of every image.

Similarly, another boxplot figure (Figure 3) was created to compare the landslides backscattering coefficient and the backscattering coefficient of all images. This was similar to backscatter analysis used by Mahdianpari et al. (2017).

##### 3.1.2 Quad Pol

We processed an L-band UAVSAR image (Rosen et al., 2006) of the Purace Volcano (Colombia), acquired in March 13, 2015, in the free access software PolSAR pro v.5.0. First, the coherence matrix (T3) was obtained (Shibayama et al., 2013)), that later generated the decomposition of the Alpha, Entropy and Anisotropy images that were needed after to proceed with the unsupervised H/a/lambda decomposition (Li et al., 2017), this decomposition gave the classification of 27 classes showed in a plane (Figure 6).

Dispersion mechanisms are quantifying by coding radar signal in a matrix of dispersion (Eq 1). Nine elements of T3 matrix are calculated for each pixel on image.

$$[T3] = \begin{pmatrix} \langle |S_{HH} + S_{VV}|^2 \rangle & \langle (S_{HH} + S_{VV})(S_{HH} - S_{VV})^* \rangle & 2\langle (S_{HH} + S_{VV})S_{HV}^* \rangle \\ \langle (S_{HH} - S_{VV})(S_{HH} + S_{VV})^* \rangle & \langle |S_{HH} - S_{VV}|^2 \rangle & 2\langle (S_{HH} - S_{VV})S_{HV}^* \rangle \\ 2\langle S_{HV}(S_{HH} + S_{VV})^* \rangle & 2\langle S_{HV}(S_{HH} - S_{VV})^* \rangle & 4\langle |S_{HV}|^2 \rangle \end{pmatrix} \quad (1)$$

By polarimetric decomposition a set of parameters are obtained to classify dispersion mechanisms. Eigen values and eigen vectors were derivate from T3 matrix as shown in Equation 2 (Eq 2) and Equation 3 (Eq 3) (Yonezawa et al., 2012).

$$[T] = [U_3] \begin{pmatrix} \lambda_1 & 0 & 0 \\ 0 & \lambda_2 & 0 \\ 0 & 0 & \lambda_3 \end{pmatrix} [U_3]^*T \quad (2)$$

$$[U_3] = \begin{pmatrix} \cos \alpha_1 & \cos \alpha_2 & \cos \alpha_3 \\ \sin \alpha_1 \cos \beta_1 e^{i\delta_1} & \sin \alpha_2 \cos \beta_2 e^{i\delta_2} & \sin \alpha_3 \cos \beta_3 e^{i\delta_3} \\ \sin \alpha_1 \sin \beta_1 e^{i\gamma_1} & \sin \alpha_2 \sin \beta_2 e^{i\gamma_2} & \sin \alpha_3 \sin \beta_3 e^{i\gamma_3} \end{pmatrix} \quad (3)$$

Eigen values ( $\lambda$ ) are used to calculate entropy (H) which is function of noise due to the polarisation, Equation 4.

$$H = \sum_{i=1}^3 p_i \log_3 p_i \quad (4)$$

$$0 \leq H \leq 1$$

$$p_i = \frac{\lambda_i}{\sum_{q=1}^3 \lambda_q}$$

Eigen vectors contain  $\alpha$  parameter representing the dominant dispersion mechanism Equation 5, isotropic surface ( $\alpha = 0^\circ$ ), dipole volume ( $\alpha = 45^\circ$ ) and isotropic dihedral ( $\alpha = 90^\circ$ ).

$$\alpha = \sum_{i=1}^3 p_i \alpha_i \quad (5)$$

$$0 \leq \alpha \leq \frac{\pi}{2}$$

### 3.1.3 Weight of Evidence (WofE) and Logistic Regression analysis

Using Spatial Data Modeller Extension for ArcView and Spatial Analysis (ArcSDM) of Arc View GIS 3.2 (Kemp et al., 2001), the weights of evidence (Neuhäuser et al., 2007) and logistic regression (Eker et al., 2016) were run. We obtained the strength of each SAR parameter for predicting landslide susceptibility and a model of landslide probability was obtained by binary logistic regression.

### 3.2 Data

Main characteristics of L1 radar images are in Table 1. UAVSAR images have longer wavelength and better spatial resolution and four polarisations.

Radar image	Band/ $\lambda$	SR (m)	GRD image	PolSAR
Sentinel-1 (ascending orbit)	C/6 cm	14	S1A1C60(20150512)	VH/VV
			S1B2EDC (20161120)	
			S1B9006 (20170730)	
			S1BBA6C (20170811)	
UAVSAR	L/27 cm	6	CoVol_31800_15019_006_150313_L090_CX_01 (20150313)	VH/VV /HV/HH

Table 1. Characteristics of Sentinel-1 and UAVSAR images

## 4. STUDY AREA

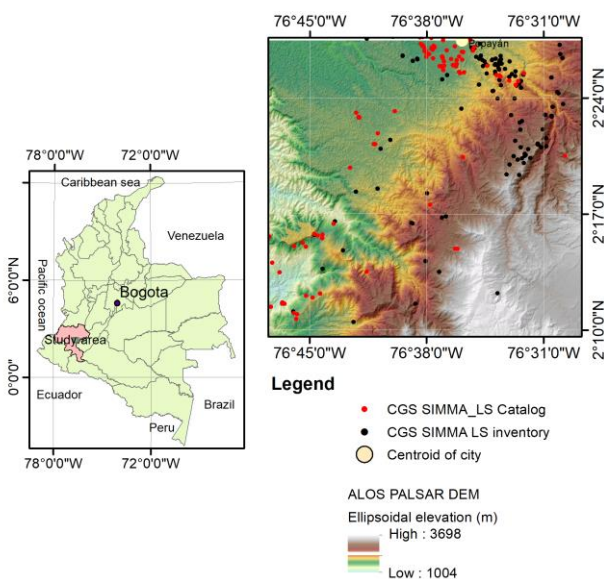


Figure 1. Study area.

The study area is a rectangle with the WGS84 coordinates of 02°09'36.66" North, 76°47'38.79" West and 02°28'11.91" North, 76°27'56.38" West, with an area of 45 km x 30 km (1350 km<sup>2</sup>). This zone is in south-eastern Colombia (Figure 1). The Mass Movement Information System (SIMMA) of Colombian Geological Service provided a database of landslides with 181 events of inventory and 248 events of catalogue type. The first inventory had a landslide distribution

of 20,4% of fall, 71,3% of slide, 4,4% of reputation, 3,3% of flow and 0,6% of lateral spread. The zone is located into a transect which contains heights between 1004 and 3698 m on the Andes mountains.

## 5. RESULTS

### 5.1 Dual Pol

#### 5.1.1 Overall distribution of backscatter

Using dual-pol, we found the backscatter calibration coefficients for four GRD Sentinel-1 radar images acquired on the dates 5th Dec 2015, 20th Nov 2016, 30th July 2017 and 11th Aug 2017. The acquisition time interval varies from 351, 252 and 12 days respectively. The boxplot (Figure 2) gave information about the distribution of calibrated backscatter in separate times and dual-polarisation. The overall distribution of backscatter is as follows: for VH polarisation, an overall range between -22,24 dB and -3,21 dB, an average median about -15 dB was found. In relation to VV polarisation, the range varied between -18,68 dB and 3,17 dB. The average median is about -9,27 dB. These values indicate that the dominant scattering mechanism is the surface dispersion on opened areas. On the other hand, the backscatter calibration distribution has positive asymmetry where there are high values with low frequency. VH and VV C-band polarisation in VH2EDC, VH9006 y VHBA6C radar images, showed no significant differences between the backscatter mean values, (p-value > 0,05). The highest correlation was found between VH2EDC and VH9006 GRD radar images ( $r=0,91$  for VH and  $r=0,94$  for VV polarisation).

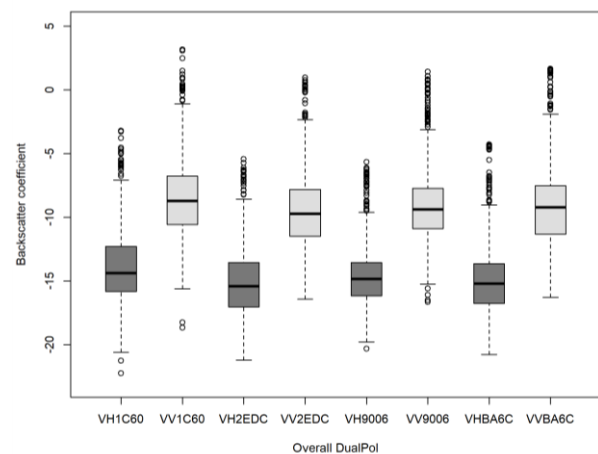


Figure 2. Backscatter of all ground scatterers

#### 5.1.2 Specific distribution of landslide backscatter

The following figure (Figure 3) showed the changes of calibrated backscatter of landslides, over a period of two years. S1B-ABA6C radar image did not appear because it did not cover the region within the landslides database. By the T-Test, we demonstrated the equality of means (p-value > 0,05) in the three GRD radar images. In VH polarisation, landslides emit a calibrated backscatter between -19,30 to -8,80 dB, with a median of -14,47 dB. This interval increased from -14,15 to -0,51 dB, with a median of -8,25 dB for VV polarisation. In overall terms, the average backscattering coefficient corresponds to -14,47 dB for VH polarisation and -8,46 dB VV

polarisation. The distribution of VH polarisation is more homogenous than VV polarisation ( $CV_{VH}=15,3\%$  against  $CV_{VV}=31,3\%$ ). Both VH and VV distributions, reported a low positive skewness (0,20 and 0,35), with some outliers in the upper region of the distribution.

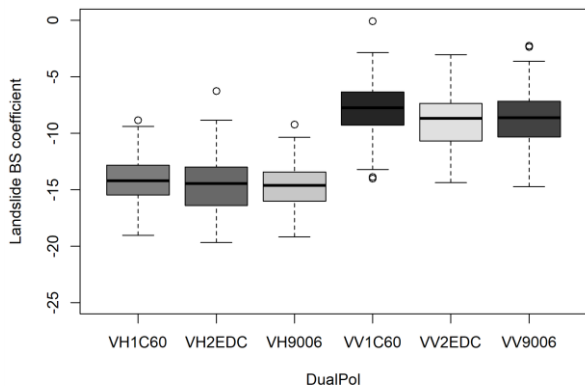


Figure 3. Backscatter over landslide scatters

### 5.1.3 Weight of evidence (WofE) analysis

Two GRD L1 radar images were selected (S1A-1C60, S1B-9006) because they covered most of the landslide distribution zone. Using ArcView GIS 3.2, an WofE analysis and logistic regression (LR) was performed. The most representative results were found in the S1A-1C60 GRD L1 image of May 12th, 2015. The figure 4, presents the posterior logistic regression probability where GRD L1 image covered the major part of local landslides. Although, the maximum probability in the landslides susceptibility map is about 0,43, the results showed concordance with spatial distribution with landslide inventory.

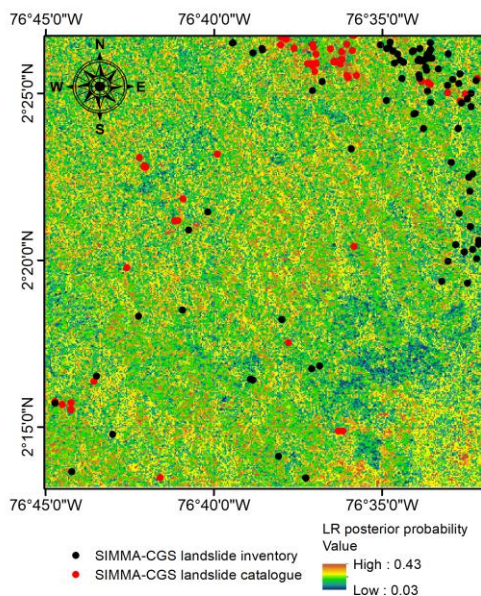


Figure 4. LR Posterior Probability obtained with S1-1C60 GRD L1 DualPol

The binary logistic regression is expressed in a math way as it's indicated in the following equation:

$$LSsusceptibility = \text{Logit}(p) = -2.805879 - 0.368401 \times (1C60_{VH}) + 0.431977 \times (1C60_{VV}) \quad (6)$$

The VH backscatter calibrated of -16,67 dB to -15,0 dB has the highest Studentized contrast (stud(C)) (Table 2) which indicated that this BS category is more susceptible to landslides. The VV backscatter calibrated between -10,17 dB and -7,97 dB gave the highest Studentized contrast (stud(C)) (Table 3) which indicates that this BS category is more susceptible to landslides in this polarimetry.

Class	BS	#LS	W+	W-	C	S(C)	Stud(C)
1	-18,3 / -16,7	6	0,12	-0,01	0,13	0,46	0,29
2	-16,7 / -15,0	19	0,38	-0,12	0,50	0,29	1,71
3	-15,0 / -13,4	16	-0,25	0,10	-0,35	0,30	-1,15
4	-13,4 / -11,7	15	-0,03	0,01	-0,04	0,31	-0,12
5	-11,7 / -10	7	-0,03	0,004	-0,04	0,42	-0,09
6	-10 / 8,4	4	0,47	-0,02	0,49	0,56	0,87

Table 2. Spatial relationship between landslide VH-BS and SIMMA landslide inventory.

Class	BS	#LS	W+	W-	C	S(C)	Stud(C)
1	-12,4 / -10,2	7	0,32	0,05	0,36	0,42	0,87
2	-10,2 / -8,0	26	0,29	-0,15	0,44	0,27	1,66
3	-8,0 / -5,8	19	-0,05	0,02	-0,08	0,29	-0,26
4	-5,8 / -3,6	10	-0,01	0,002	-0,01	0,36	-0,04
5	-3,6 / -1,4	4	0,11	-0,006	0,11	0,55	0,20
6	-1,4 / 0,9	1	0,05	-0,001	0,05	1,07	0,04

Table 3. Spatial relationship between landslide VV-BS and SIMMA landslide inventory.

The intervals found by logistic regression with greater association to the landslides corresponds to the outlined tendency measures of the backscatter distributions, especially in the VV polarization.

The median values, found for both polarisation, were located between the lowest backscatter values for water coverage (-20 dB for C-band HH and -23 dB for C-band HV) and highest backscatter values for urban class (0 dB for HH polarized data). Furthermore, upland class had a median about -10 dB in C-band. Those were investigated by Mahdianpari et al., (2017).

## 5.2 Quad-polarisation data

The objective of using fully polarimetric SAR data from UAVSAR airborne sensor, is to evaluate the effect of polarimetric descriptors on landslides classification.

### 5.2.1 Entropy – alpha parameter decomposition

Figure 5, shows the first plane of principal components analysis for Entropy – Alpha angle parameters obtained by Cloude-Pottier decomposition (Cloude et al., 1997), which measures and transforms the information of ground targets into deterministic targets (Mahdianpari et al., 2018). The parameters correctly represented in the first factorial plane of PCA analysis

are: entropy (H), alpha angle ( $\alpha$ ) and anisotropy (A). Alpha angle ( $\alpha$ ) and entropy (H) parameters had a correlation coefficient of about 0,73. Anisotropy in comparison with combination of Entropy-alpha classification also had a high relationship of about 0,85. This multivariate behaviour explains the use of unsupervised classification scheme for identifying the dominant scattering mechanism, based on entropy-alpha values (Cloude et al., 1997).

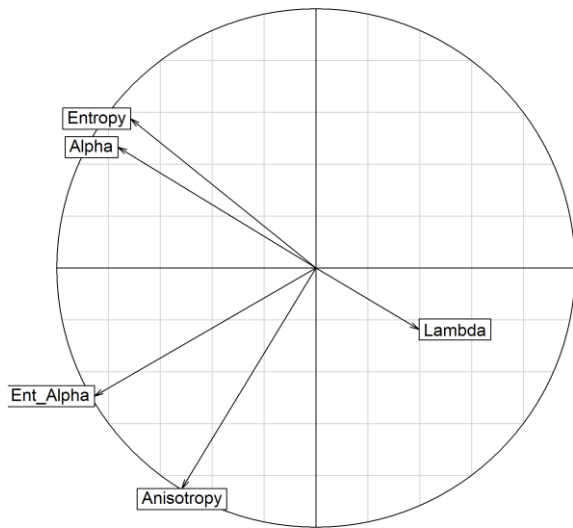


Figure 5. First factorial plane of principal component analysis for Quad-Pol parameters.

### 5.2.2 Full PolSAR classification scheme

Figure 6, shows the results of H- $\alpha$  decomposition for all scatters existing on the study area. In general, most scatters correspond to the surface and volume diffusion mechanism.

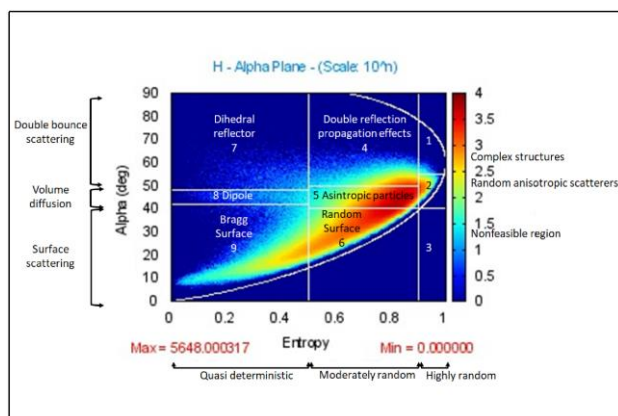


Figure 6. H-alpha distribution, using all scatters.

Table 4 shows the H- $\alpha$  decomposition distribution corresponding only to landslides scatterers. Exactly 14,6% corresponds to the double reflection propagation effects (zone 4: medium entropy multiple scattering), 42,7% of anisotropic particles (zone 5: medium entropy vegetation scattering), and 34,1% of the random surface (zone 6: medium entropy surface

scatter). Most landslides are classified in anisotropic particles which would include scattering from vegetated surfaces; others are characterized as random surface because the entropy increases due to canopy propagation effects (Cloude et al., 1997). These events are rotational, translational slides, and a few detritus falls, but if being a random surface class, most landslides types correspond to translational slides. Double reflection propagation is characterized by translation and rotational slides in equal proportion.

H- $\alpha$ class	LS number	Percentage (%)	Classification
4	12	14,6	Double reflection propagation effects
5	35	42,7	Anisotropic particles
6	28	34,1	Random surfaces
8	3	3,7	Dipole
9	4	4,9	Bragg surface

Table 4. Categories of H-alpha classification for all scatters.

The figure 7, shows the spatial distribution of landslide classification according to the alpha parameter. The results showed that the scatter mechanism has the following distribution: 39% for surface scattering, 46.4% for volume diffusion, and 14.6% for double bounce scattering.

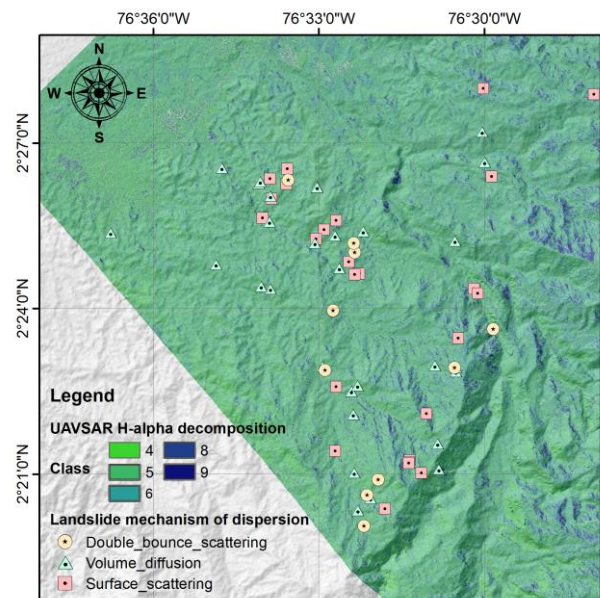


Figure 7. Landslides mechanism of dispersion using H-alpha classification.

The aforementioned means that the landslides does not always reflects surface scattering clearly, so surface and volume scattering can change in relation to variation of the observed geometries, as stated by Shibayama et al., (2015).

### 5.2.3 Landslide susceptibility with Quad-Pol parameters

To find a relationship between Quad-pol parameters and landslide events a regression analysis with binary logistic regression was performed. First, one WofE analysis was run using ArcView Gis 3.2 to obtain a value range with higher

relationship to landslides. Table 5 shows the main WofE values for some Quad-pol parameters. The most significant quad-pol parameters were: H-A-Lambda classification (Studentized contrast of 4.37, 2.94 and 3.29).

QuadPol parameter	Range	Studentized contrast of WofE method
Alpha	5,145 – 12,985	1.89
Anisotropy	0,10 – 0,20	1.32
Combination 1mH1mA1	0,09 – 0,18	1.01
Combination 1mHA1	0,44 – 0,53	1.23
Combination H1mA1	0,39 – 0,48	1.96
Combination HA	0,26 – 0,33	1.31
Entropy	0,60 – 0,70	1.98
H-A-Lambda	3,6 – 6,2	4.37
H-A-Lambda class 1	5,4 – 6,3	2.94
H-A-Lambda class 2	0 – 1,8	3.29
H-A-Lambda class 3	24,3 – 27,0	1.03

Table 5. Studentized contrast of the WofE method for more representative parameters.

Alpha angles values between 5° and 13° with Entropy values between 0.6 and 0.7, corresponds to Zone 6 of SAR classification scheme of Cloude & Pottier (1997) where the surface cover have oblate spheroidal scatterers such as canopy.

Several maps with logistic regression posterior probability were obtained by different alternatives (Table 6). The 6th alternative with QuadPol parameters (Anisotropy, Combination (1mH1mA1, 1mHA1, H1mA1, HA), Entropy) gave the highest odd range, and a conditional independence ratio of 0.93, demonstrating the independence of the variables. However, the landslide susceptibility was very low by analysing only quadpol parameters. Despite of having a high spatial resolution with UAVSAR images for quadpol analysis, these results didn't show a meaningful relationship to landslides.

Alternative	QuadPol parameters involved	Conditional Independence Ratio	Odds range of LR posterior probability
1	Alpha, Anisotropy, Entropy	1	0.004 – 0.024
2	H-Alpha-Lambda classification (Class 0, 1, 2, 3)	0.56	0.009 – 0.058
3	Combination (1mH1mA1, 1mHA1, H1mA1, HA)	0.98	0.010 – 0.039
4	Alpha, Anisotropy, Combination (1mH1mA1, 1mHA1, H1mA1, HA), Entropy	0.92	0.001 – 0.085
5	Alpha, Entropy,	1	0.004 – 0.023
6	Anisotropy, Combination (1mH1mA1, 1mHA1, H1mA1, HA), Entropy	0.93	0.003 – 0.086
7	Anisotropy, Combination 1mH1mA1, Entropy	0.98	0.008 – 0.034

Table 6. Results of LR posterior probability for QuadPol parameters.

## 6. CONCLUSIONS

Using C-band Sentinel-1 radar images, spanning the period from May 2015 to September 2017, it was possible obtain a first preliminary characterization of landslides based on its backscatter coefficient. VH and VV C-band polarised radar energy emits median values of BS, for landslides, about of -14.47 dB for VH polarisation and -8.46 dB for VV polarisation.

Using airborne L-band fully polarimetric UAVSAR data, with four polarisations, the mechanism of dispersion was found. This mechanism for landslides inventory provided by CGS landslide inventory was: 39% for surface scattering, 46.4% for volume dispersion and 14.6% for double bounce scattering. In opposition to our expectations of landslides only emitting backscattered energy through the surface mechanism, these results imply a bigger refinement in the analysis considering the geometric parameter of the radar measurement (angle of incidence) to establish this effect. However, through binary logistic regression, a good relation was found between low values of the alpha angle (5 ° to 12 °) and intermediate values of entropy (0.6 to 0.7), which correspond to zone 6, of the non-supervised classification scheme by Cloude and Pottier.

Because the C-band and L-band L1-SAR images were acquired in different years than the landslides inventory report, is necessary to follow this preliminary investigation, by using of a multi-temporal approach with images closer to the dates of occurrence of the events, and thus establishing the accuracy of the classifications obtained with the PolSAR.

## REFERENCES

- Adiri, Z., El Harti, A., Jellouli, A., Lhissou, R., Maacha, L., Azmi, M., ... Bachaoui, E. M. (2017). Comparison of Landsat-8, ASTER and Sentinel 1 satellite remote sensing data in automatic lineaments extraction: A case study of Sidi Flah-Bouskour inlier, Moroccan Anti Atlas. *Advances in Space Research*, 60(11), 2355–2367. <https://doi.org/10.1016/j.asr.2017.09.006>
- Casagli, N., Frodella, W., Morelli, S., Tofani, V., Ciampalini, A., Intrieri, E., ... Lu, P. (2017). Spaceborne, UAV and ground-based remote sensing techniques for landslide mapping, monitoring and early warning. *Geoenvironmental Disasters*, 4(9), 1–23. <https://doi.org/10.1186/s40677-017-0073-1>
- Cloude, S., & Pottier, E. (1997). An entropy based classification scheme for land applications of polarimetric SAR. *IEEE Transactions on Geoscience and Remote Sensing*, 35(1), 68–78. <https://doi.org/10.1109/36.551935>
- Colesanti, C., & Wasowski, J. (2006). Investigating landslides with space-borne Synthetic Aperture Radar (SAR) interferometry. *Engineering Geology*, 88(3–4), 173–199. <https://doi.org/10.1016/j.enggeo.2006.09.013>
- Eker, R., & Aydin, A. (2016). Landslide Susceptibility Assessment of Forest Roads \*. 2(November), 54–60.
- García-Davalillo, J. C., Herrera, G., Notti, D., Strozzi, T., & Álvarez-Fernández, I. (2014). DInSAR analysis of ALOS PALSAR images for the assessment of very slow landslides: The Tena Valley case study. *Landslides*,

- 11(2), 225–246. <https://doi.org/10.1007/s10346-012-0379-8>
- Han, D., Vahedifard, F., & Aanstoos, J. V. (2017). Investigating the correlation between radar backscatter and in situ soil property measurements. *International Journal of Applied Earth Observation and Geoinformation*, 57, 136–144. <https://doi.org/10.1016/j.jag.2016.12.018>
- Kemp, L. D., Bonham-Carter, G. F., Raines, G. L., & Looney, C. G. (2001). *Arc-SDM: Arcview extension for spatial data modelling using weights of evidence, logistic regression, fuzzy logic and neural network analysis*. São Paulo: Instituto de Geociências, Universidade Estadual de Campinas. Retrieved from <http://www.ige.unicamp.br/sdm/>
- Li, D., & Zhang, Y. (2017). Random Similarity-Based Entropy/Alpha Classification of PolSAR Data. *IEEE Journal of Selected Topics in Applied Earth Observations and Remote Sensing*, 10(12), 5712–5723. <https://doi.org/10.1109/JSTARS.2017.2748234>
- Mahdianpari, M., Salehi, B., Mohammadimanesh, F., Brisco, B., Mahdavi, S., Amani, M., & Granger, J. E. (2018). Fisher Linear Discriminant Analysis of coherency matrix for wetland classification using PolSAR imagery. *Remote Sensing of Environment*, 206(October 2017), 300–317. <https://doi.org/10.1016/j.rse.2017.11.005>
- Mahdianpari, M., Salehi, B., Mohammadimanesh, F., & Motagh, M. (2017). Random forest wetland classification using ALOS-2 L-band, RADARSAT-2 C-band, and TerraSAR-X imagery. *ISPRS Journal of Photogrammetry and Remote Sensing*, 130, 13–31. <https://doi.org/10.1016/j.isprsjprs.2017.05.010>
- Matikainen, L., Lehtomäki, M., Ahokas, E., Hyyppä, J., Karjalainen, M., Jaakkola, A., ... Heinonen, T. (2016). Remote sensing methods for power line corridor surveys. *{ISPRS} Journal of Photogrammetry and Remote Sensing*, 119, 10–31. <https://doi.org/http://dx.doi.org/10.1016/j.isprsjprs.2016.04.011>
- Mondini, A. (2017). Measures of Spatial Autocorrelation Changes in Multitemporal SAR Images for Event Landslides Detection. *Remote Sensing*, 9(6), 554. <https://doi.org/10.3390/rs9060554>
- Neuhäuser, B., & Terhorst, B. (2007). Landslide susceptibility assessment using “weights-of-evidence” applied to a study area at the Jurassic escarpment (SW-Germany). *Geomorphology*, 86(1–2), 12–24. <https://doi.org/10.1016/j.geomorph.2006.08.002>
- Notti, D., Davalillo, J. C., Herrera, G., & Mora, O. (2010). Assessment of the performance of X-band satellite radar data for landslide mapping and monitoring: Upper Tena Valley case study. *Natural Hazards and Earth System Science*, 10(9), 1865–1875. <https://doi.org/10.5194/nhess-10-1865-2010>
- Ouchi, K. (2013). Recent trend and advance of synthetic aperture radar with selected topics. *Remote Sensing*, 5(2), 716–807. <https://doi.org/10.3390/rs5020716>
- Plank, S., Twele, A., & Martinis, S. (2016). Landslide Mapping in Vegetated Areas Using Change Detection Based on Optical and Polarimetric SAR Data. *Remote Sensing*, 8(4), 307. <https://doi.org/10.3390/rs8040307>
- Richards, J. a. (2009). *Remote Sensing with Imaging Radar*. Canberra: Springer. <https://doi.org/10.1007/978-3-642-02020-9>
- Rocca, F., & Ferretti, A. (2014). An Overview of SAR Interferometry, 1–13. Retrieved from <https://earth.esa.int/workshops/ers97/program-details/speeches/rocca-et-al/>
- Rosen, P., Hensley, S., Wheeler, K., Sadowy, G., Miller, T., Shaffer, S., ... Madsen, S. (2006). UAVSAR: a new NASA airborne SAR system for science and technology research. *Proc. 2006 {IEEE} Conf. on Radar*, 22–29.
- Scaioni, M., Longoni, L., Melillo, V., & Papini, M. (2014). Remote Sensing for Landslide Investigations: An Overview of Recent Achievements and Perspectives. *Remote Sensing*, 6(7), 5909–5937. <https://doi.org/10.3390/rs60x000x>
- Shibayama, T., & Yamaguchi, Y. (2013). AN APPLICATION OF POLARIMTRIC RADAR ANALYSIS Graduate School of Science and Technology, Niigata University, Japan. *International Geoscience and Remote Sensing Symposium (IGARSS)*, (1), 3191–3194.
- Shibayama, T., Yamaguchi, Y., & Yamada, H. (2015). Polarimetric scattering properties of landslides in forested areas and the dependence on the local incidence angle. *Remote Sensing*, 7(11), 15424–15442. <https://doi.org/10.3390/rs71115424>
- Shimada, M., Itoh, T., Motooka, T., Watanabe, M., Shiraishi, T., Thapa, R., & Lucas, R. (2014). New global forest/non-forest maps from ALOS PALSAR data (2007–2010). *Remote Sensing of Environment*, 155, 13–31. <https://doi.org/10.1016/j.rse.2014.04.014>
- Sun, W., Tian, Y., Mu, X., Zhai, J., Gao, P., & Zhao, G. (2017). Loess Landslide Inventory Map Based on GF-1 Satellite Imagery. *Remote Sensing*, 9(314), 1–17. <https://doi.org/10.3390/rs9040314>
- Tansey, J., & Millington, A. C. (2001). Investigating the potential for soil moisture and surface roughness monitoring in drylands using ERS SAR data. *International Journal of Remote Sensing*, 22(11), 2129–2149. <https://doi.org/10.1080/01431160121099>
- Tehrany, M. S., Kumar, L., & Drielsma, M. J. (2017). Review of native vegetation condition assessment concepts, methods and future trends. *Journal for Nature Conservation*. <https://doi.org/10.1016/j.jnc.2017.08.004>
- Tessari, G., Floris, M., & Pasquali, P. (2017). Phase and amplitude analyses of SAR data for landslide detection and monitoring in non-urban areas located in the North-Eastern Italian pre-Alps. *Environmental Earth Sciences*, 76(2), 85. <https://doi.org/10.1007/s12665-017-6403-5>
- Vogeler, J. C., & Cohen, W. B. (2016). A review of the role of active remote sensing and data fusion for characterizing forest in wildlife habitat models. *Spanish Association of Remote Sensing*, 45, 1–14.
- Wilson, J. P. (2012). Digital terrain modeling. *Geomorphology*, 137(1), 107–121. <https://doi.org/10.1016/j.geomorph.2011.03.012>
- Yague-martinez, N., Prats-iraola, P., Member, S., Gonzalez, F. R., Brcic, R., Shau, R., ... S-, A. S-. (2016). Interferometric Processing of Sentinel-1 TOPS Data. *IEEE Transactions on Geoscience and Remote Sensing*, 54(4), 2220–2234.
- Yonezawa, C., Watanabe, M., & Saito, G. (2012). Polarimetric decomposition analysis of ALOS PALSAR observation data before and after a landslide event. *Remote Sensing*, 4(8), 2314–2328.